HE-OD spectroscopy of supercontinuum generation

May 30, 2012

Abstract

1 Introduction

2 Theoretical Background

2.1 Full propagation equations

Let us consider the propagation along z of an electric field E linearly polarized along a direction $\overrightarrow{u_x}$ with a cylindrical symmetry with respect to the propagation direction $\overrightarrow{u_z}$: $\overrightarrow{\mathrm{E}}(\mathrm{r,z,t})=\frac{1}{2}\left[\varepsilon(\mathrm{r,z,t})+\varepsilon^*(\mathrm{r,z,t})\right]\overrightarrow{u_x}$

Following the UPPE derivation [1], in a frame propagating at a velocity v_g, and ignoring both harmonic generation and backward propagating field, the scalar complex electric field ε evolves as:

$$\begin{aligned}\partial_z\widetilde{\varepsilon} &= \mathrm{i}(\mathrm{k}_z-\frac{\omega}{\mathrm{v_g}})\widetilde{\varepsilon}-\widetilde{\mathrm{L}}_{\mathrm{loss}}+\frac{\omega}{\mathrm{c}^2\mathrm{k}_z}\times \\ &\left[i\omega(\sum \mathrm{n}_{2\mathrm{j}}\widetilde{|\varepsilon|^{2\mathrm{j}}\varepsilon}+\Delta\mathrm{n}_{\mathrm{vr}}(\omega)\widetilde{\varepsilon})-\frac{\mathrm{e}^2}{2\epsilon_0\mathrm{m_e}}\tau(\omega)\widetilde{\rho\varepsilon}\right]\end{aligned} \tag{1}$$

where ϵ_0 is the vacuum permittivity, c is the vacuum light velocity, e and $\mathrm{m_e}$ is the electron charge and mass respectively, ω is the absolute angular frequency, $\mathrm{k}_z=\sqrt{\mathrm{k}^2(\omega)-\mathrm{k}_\perp^2}$ with $\mathrm{k}(\omega)=\mathrm{n}(\omega)\omega/\mathrm{c}$, $\mathrm{n}(\omega)$ being the refractive

index at frequency ω and $k_\perp$ the spatial angular frequency. $\widetilde{f}$ denotes simultaneous temporal Fourier and spatial Hankel transforms of function f: $\widetilde{f} = \int_0^\infty \int_{-\infty}^\infty rJ_0(k_\perp r)f(r,t)e^{i\omega t}dtdr$, where J_0 is the zeroth order Bessel function. Moreover, n_{2j} is the j^{th} nonlinear refractive index, Δn_{vr} is the refractive index change induced by nonlinear vibrational and/or rotational effects, and $\tau(\omega) = (\nu_{en} + i\omega)/(\nu_{en}^2 + \omega^2)$ accounts for the collision spectrum with ν_{en} being the electron-neutral collision frequency.

Finally, ρ denotes the free electrons density and is evaluated as:

$$\partial_t \rho = W(|\varepsilon|^2)\,(\rho_{at} - \rho) + \frac{\sigma}{U_i}|\varepsilon|^2 - g(\rho) \tag{2}$$

where W accounts for the ionization probability, σ is the inverse Bremsstrahlung cross-section, U_i is the ionization potential of atoms, ρ_{at} is the neutral density and g is the recombination function.

Moreover, $L_{loss}=\frac{U_i W(|\varepsilon|^2)}{2|\varepsilon|^2}(\rho_{at} - \rho)\varepsilon$ accounts for losses induced by the photo-ionization process.

2.2 Approximated propagation equations

In this section, we will consider a simple "1D" model in order to roughly catch the propagation dynamics of powerful laser pulse. This dimension-reduced model is particularly useful since it allows quick calculations not feasible when using the full 2D+1 model, due to its high computational cost. Let us consider that no space-time coupling occurs during the whole propagation. Even if this simplification is not justified during the filamentation process, it allows to have a first look on the physics underlying the supercontinuum generation with short pulse.

Within this assumption, the complex electric field can be written at any propagation distance z as $\varepsilon(r,t,z) = \varphi(t,z)\psi(r,z)$ and the Fourier transform $\widetilde{\varphi}$ of φ evolves as

$$\begin{aligned}\partial_z \widetilde{\varphi} = & i\left[k(\omega) - \frac{\omega}{v_g}\right]\widetilde{\varphi} + i\frac{k(\omega)}{n^2(\omega)}\left(n_2\widetilde{|\varphi|^2\varphi} + \Delta n_{vr}(\omega)\widetilde{\varphi}\right) \\ & - \frac{ie^2}{2n(\omega)\epsilon_0 m_e c}\tau(\omega)\widetilde{\rho\varphi} - \widetilde{L}_{loss}\end{aligned} \tag{3}$$

Reduced models

As mentioned above, the 1D model approximation allows numerical exploration of propagation effects. In particular, it is possible to isolate the effects of certain processes by neglecting some terms in Eq. 3. When only dispersion and electronic Kerr effect are taken into account, i.e., neglecting any effect induced by free electrons or molecules vibration (Raman), the 1D propagation equation reduces to

$$\partial_z\widetilde{\varphi}=\mathrm{i}\left[\mathrm{k}(\omega)\text{-}\frac{\omega}{\mathrm{v_g}}\right]\widetilde{\varphi}+\mathrm{i}\frac{\mathrm{n_2k}(\omega)}{\mathrm{n}^2(\omega)}\widetilde{|\varphi|^2\varphi}. \tag{4}$$

Ionization effects can be studied by neglecting both bounded electrons and vibrational effects. Accordingly, the equation driving the electric field propagation becomes

$$\partial_z\widetilde{\varphi}=\mathrm{i}\left[\mathrm{k}(\omega)\text{-}\frac{\omega}{\mathrm{v_g}}\right]\widetilde{\varphi}-\frac{\mathrm{ie}^2}{2\mathrm{n}(\omega)\epsilon_0\mathrm{m_e c}}\tau(\omega)\widetilde{\rho\varphi}-\widetilde{\mathrm{L}}_{\mathrm{loss}}. \tag{5}$$

The combined contribution of the Kerr effect and ionization is obtained by neglecting vibrational effects, and follows

$$\begin{aligned}\partial_z\widetilde{\varphi}=\mathrm{i}\left[\mathrm{k}(\omega)\text{-}\frac{\omega}{\mathrm{v_g}}\right]\widetilde{\varphi}+\mathrm{i}\frac{\mathrm{n_2k}(\omega)}{\mathrm{n}^2(\omega)}\widetilde{|\varphi|^2\varphi}\\ -\frac{\mathrm{ie}^2}{2\mathrm{n}(\omega)\epsilon_0\mathrm{m_e c}}\tau(\omega)\widetilde{\rho\varphi}-\widetilde{\mathrm{L}}_{\mathrm{loss}}.\end{aligned} \tag{6}$$

2.3 HE-OD

HE-OD is an encoding-decoding technique that aids in the extraction of mechanistic information from nonlinear systems. For a nonlinear system that produces an output signal O upon excitation by an ultrafast laser field $E(t)$, HE-OD consists in inserting perturbations into the laser field phase and retrieving the perturbed output signal from the nonlinear system. The process requires m separate experiments each labeled by the parameter $s = 1, \ldots, m$. The perturbations take the form of added phases $f_k(s), k = 1, \ldots, M$, to groups of selected spectral components of the field, producing a modulated

output signal $O(s)$. The encoded field is given by

$$E_s(t) = C_0(t) + \sum_{k=1}^{M} C_k(t) e^{i\omega_k t} e^{i f_k(s)} + c.c., \tag{7}$$

where, $\omega_k, k = 1, \ldots, M$ are the angular frequencies around which the encoding is applied and $C_k(t), k = 0, \ldots, M$ are slowly varying functions. As a result of interaction with the nonlinear system, the spectral components of the field are mixed. Moreover, if the field propagates through the nonlinear system, previously mixed light can in turn mix again with the rest of the field. In general, the output modulated signal is of the form

$$O(s) = \sum_{n_1,\ldots,n_M} P(n_1, \ldots, n_M) \times h\left(n_1, \ldots, n_M; s\right), \tag{8}$$

with,

$$h\left(n_1, \ldots, n_M; s\right) = e^{i[n_1 f_1(s) + \ldots + n_M f_M(s)]}, \tag{9}$$

and where, $n_1, \ldots, n_M$ are integers, and $P(n_1, \ldots, n_M), \forall n_1, \ldots, n_M$ are complex numbers that will be referred to as projections. Equation 8 expresses the fact that the modulated signal may be the result of any possible mixing of the laser field's spectral components. Indeed, a nonzero projection $P(n_1, \ldots, n_M)$ indicates that in the output signal there is a mixing of n_1-, n_2-,...,n_M−times of the expectral components around ω_1, ω_2, ..., ω_M, respectively. If the encoding functions $f_1(s), \ldots, f_M(s)$ are chosen so that for all integers n_k, n'_k, $k = 1, \ldots, M$ we have

$$\sum_{s=1}^{m} h\left(n_1, \ldots, n_M; s\right) \times h^*\left(n'_1, \ldots, n'_M; s\right) = \delta_{n_1,n'_1} \times \delta_{n_2,n'_2} \times \ldots \times \delta_{n_M,n'_M}, \tag{10}$$

where, $\delta_{nn'}$ is the delta kronecker, then the projections $P(n_1, \ldots, n_M)$ can be extracted from the modulated signal as

$$P(n_1, \ldots, n_M) = \sum_{s=1}^{m} O(s) \times h^*\left(n_1, \ldots, n_M; s\right). \tag{11}$$

The encoding functions used in the present work are defined in Sec. 7, where the orthogonality of the corresponding modulating functions, Eq. (10), is also proven.

Mechanistic insights may be extracted from the projections by incorporating additional known information about the system. For instance, in the case of a multilevel quantum system, the projections provide a system of equations from which quantum pathway amplitudes can be obtained [2, 3]. As shown below, in the context of a nonlinear system that undergoes light propagation, a rough knowledge of the order of the various nonlinear interactions present in the system can assist in the interpretation of the experimentally extracted projections.

3 Experimental Implementation

3.1 Experimental setup

The setup is shown in Figure 1. The experiments utilized a Spectra Physics Ti:sapphire femtosecond laser consisting of a Tsuami oscillator and a 1 kHz Spitfire amplifier. The amplified pulses had a spectrum with full width at half maximum (FWHM) of ∼12 nm centered at 793 nm (see Figure 2), corresponding to a transform-limited temporal pulse width of ∼ 70 fs FWHM. Phase modulation was performed with a 4-f configuration pulse shaper having a liquid crystal display (LCD) with 128 pixels (CRI-SLM), as shown in Figure 1. The output from the pulse shaper was attenuated to an energy of 0.5 μJ and focused by a f = 8 cm lens onto a 2 mm Sapphire plate. The generated white light beam was then directed to an apperture to remove the outer rings. The spectrum of central part of the beam was then measured by an Ocean Optics HR-2000 (800-nm) spectrometer. The original phase (before HE-OD modulation) of the field $E(t)$ corresponded to a SLM phase equal to zero, which approximately produced transform-limited pulses.

3.2 Field encoding

Spectral components in the intervals 796.5 nm $< \lambda <$ 798.5 nm and 787.5 nm $< \lambda <$ 789.5 nm were encoded by adding to their phases $f_1(s)$ and $f_2(s)$, respectively. Figure 2 illustrates the position of the encoded intervals in relation with the laser spectrum.

The encoding functions $f_1(s)$ and $f_2(s)$ were constructed as specified in Sec. 7 with m = 16,384 points (see Figure 3). Section 7 shows that $f_1(s)$ and $f_2(s)$ generate an orthogonal set of modulating functions $\{h(n_1, n_2; s)\}$

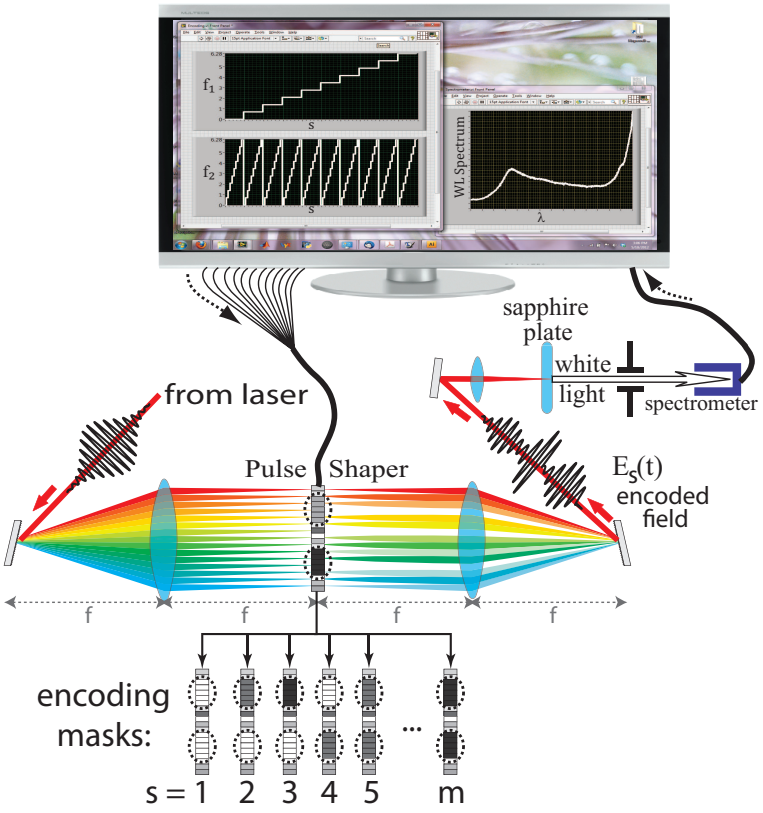

Figure 1: Experimental setup.

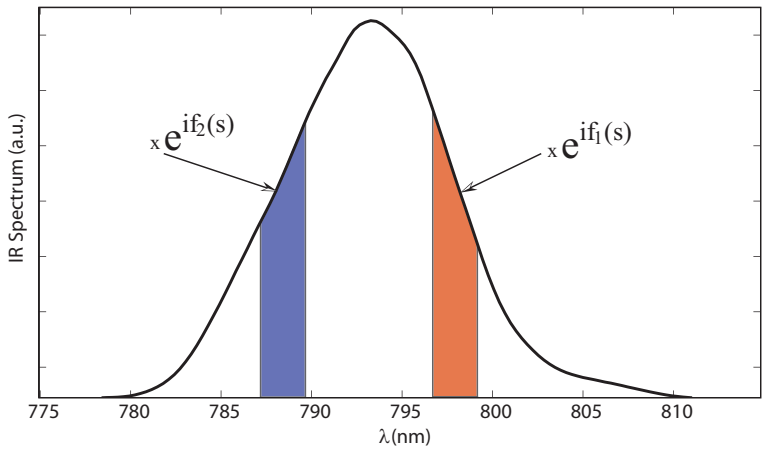

Figure 2: Input laser spectrum (solid line). The portions of the spectrum encoded by $f_1(s)$ and $f_2(s)$ are indicated by red and blue areas, respectively.

(see Eq. 9).

3.3 Modulated signal

The modulated white light spectrum resulting from the encoding described in Sec. 3.2 is shown in Figure 4.

3.4 Decoded projections

The modulated white ligth signal was decoded using Eq. (refEq:ExtractProjs) to yield the projections $P(n_1, n_2)$ as a function of wavelength. Figure 5 shows the amplitudes of the extracted projections as a function of wavelength and projection order. The order of projection $P(n_1, n_2)$ is defined as $|n_1|+|n_2|$. In general, the projection amplitude decreases for increasing projection orders. The highest-order projections (projection order > 15) appear for white light wavelengths of ~ 550 nm.

Figure 6 shows the wavelength dependence of selected projection amplitudes. Notice the ~ 50 nm oscillations present in the projections.

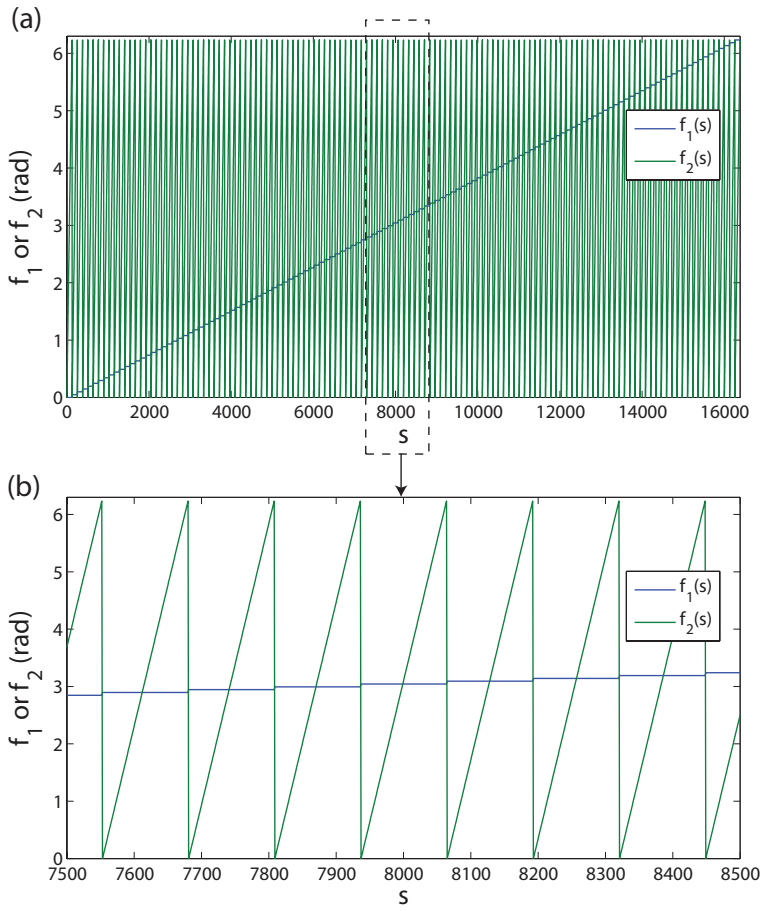

Figure 3: Encoding functions $f_1(s)$ (blue) and $f_2(s)$ (green) used in the experiments shown over their full range (a), and zoomed in (b) to aid in showing their structure. The dashed-line rectangle in (a) indicates the zoomed range shown in (b). Both $f_1(s)$ and $f_2(s)$ take 128 discrete values between 0 and 2π but they are arranged so that for each value of $f_1(s)$, the other function $f_2(s)$ takes on all its possible values in succesion, for a total of $128^2 = 16,384$ points. More details are given in Sec. 7.

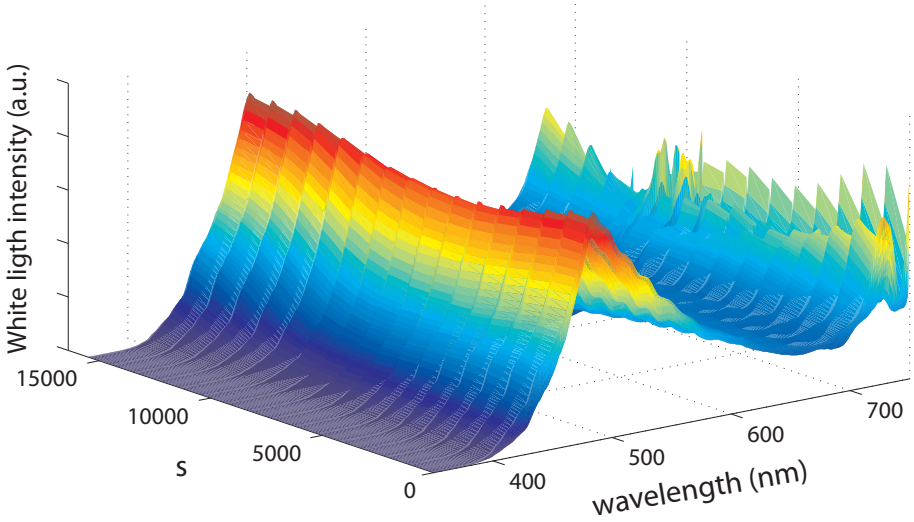

Figure 4: Measured white light as a function of wavelength and the encoding parameter s.

4 Numerical Simulations

Information about the light-matter processes that take place during supercontinuum generation can be inferred from the experimentally extracted projections' spectra presented in Sec. 3. We show here the results of numerical simulations using parameters similar to the experimental parameters. One of the goals of this section is to numerically recreate the HE-OD experimental signal using the known propagation equations (see Eqs. (1) and (2)). Some features of the experimental data can be attributed to specific processes. Thus, it is possible to approximately isolate part of the dynamics, focussing on certain processes in order to fine tune the simulation parameters to reproduce the experimental features. This is accomplished by solving the 1D models of Sec. 2.2 with some processes turned off. Solving the 1D models is numerically inexpensive, allowing the testing of a range of simulation parameters. All the simulations use the material parameters of fused silica (instead of sapphire), but there is good agreement with the experimental data, as shown below.

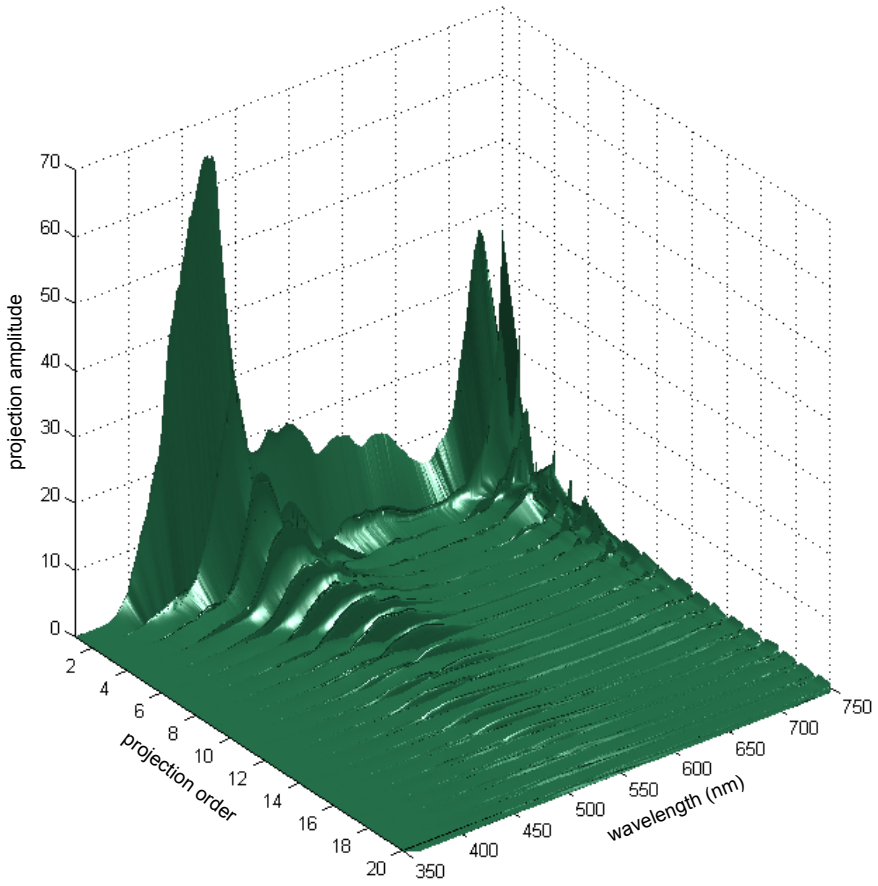

Figure 5: Amplitudes of the complex projections extracted from the experimental data as a function of wavelength and projection order. Due to the large number of projections $P(n_1, n_2)$ involved, the projections are grouped into orders, where the projection order is defined as $|n_1| + |n_2|$. Projection $P(0, 0)$ (proportional to the portion of the white light signal not affected by the encoding) is not shown due to it's large amplitude in relation to the remaining projections.

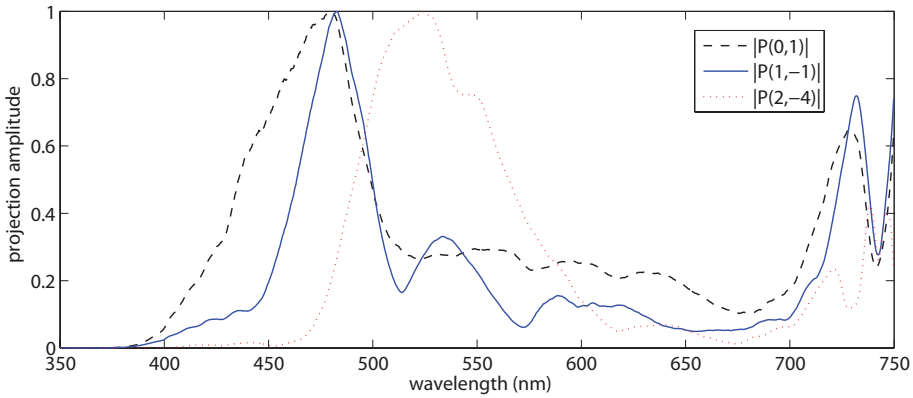

Figure 6: Wavelength dependence of selected projection amplitudes. Oscillations of ~ 50 nm appear on the projections.

4.1 Initial conditions

The incident complex electric field envelope is modeled as

$$\varepsilon(\mathrm{r,t,z=0}) = \sqrt{\mathrm{I_0}}\, \mathrm{e}^{-\frac{\mathrm{t}^2}{\sigma_\mathrm{t}^2}}\, \mathrm{e}^{-\frac{\mathrm{r}^2}{\sigma_\mathrm{r}^2}}\, \mathrm{e}^{-\mathrm{i}\frac{\mathrm{k_0 r}^2}{2\mathrm{f}}}, \tag{12}$$

with f being the focal length and $\mathrm{I_0}=\frac{2\mathrm{P}}{\pi\sigma_\mathrm{r}^2}$ where $\mathrm{P}=\sqrt{\frac{2}{\pi}}\frac{\mathrm{E}}{\sigma_\mathrm{t}}$ is the instantaneous power and E being the total energy within the pulse.

In order to mimic the experiments, we chose E=1.46 μJ, σ_t=71.7 fs (estimated from the experimental spectrum), σ_r=4.25 mm and f=8 cm. One has to emphasize that Eq. 1 overcomes the paraxial approximation and then allows to describe accurately the present experiment conditions (numerical aperture $\simeq 0.05$). Before propagating within the fused silica plate, the pulse propagates through the air considered as a linear medium. The 2 mm thick fused silica plate is placed so that the linear focus is located at the middle of the plate. Due to self-focusing, the pulse focuses slightly before (around 700 μm after the input face).

4.2 Propagation dynamics of the transform-limited pulse

In the experiments, the original (prior to any HE-OD modulation) field $E(t)$ corresponds to the transform-limited pulse (i.e., shortest pulse allowed by the laser bandwidth). To obtain general insights on the pulse's propagation

properties, we first simulated the propagation dynamics of the transform-limited pulse under the experimental conditions. As expected for instantaneous power P$\simeq$8 P_{crit} (P_{crit}=3.77$\lambda_0^2/(8\pi n_0 n_2)$), the pulse undergoes several focusing cycles during the propagation as one can notice in Fig.7(a) which displays the radial fluence distribution as a function of the propagation distance. During the filamentation process, the pulse spectrum broadens (Fig. 7(b,d)) due to nonlinearities (induced by both bounded and free electrons) to form a supercontinuum spanning from $\simeq$ 450 nm to $\simeq$ 1400 nm and the intensity within the core is clamped to about 35 TW/cm^2 (Fig. 7(c)), producing an electron density of about 4 10^{19} cm^{-3} over about 1 mm. This highly nonlinear propagation is accompanied by a strong angular-frequency reshaping, resulting in a X-wave pattern (which manifests itself by both visible and infrared conical emission) as one can notice in Fig. 8. More particularly, two X-wave are generated. The first one is centered at $\lambda = \lambda_0$ and the other at $\lambda \simeq 470\ nm$ ($\omega/\omega_0 \simeq$1.7).

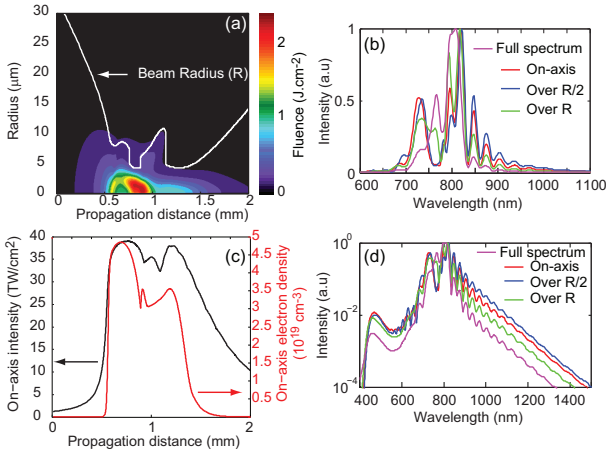

Figure 7: (a) Transverse fluence distribution along the propagation. (b) Output integrated spectra in a linear scale. (red) on-axis, (blue) integrated over an half-radius, (green) integrated over the beam radius and (pink) integrated over the full beam. (c) The black (red) line corresponds to the peak intensity (peak electron density) along the propagation. (d) Same than (b) but in a logarithmic scale

The white light spectrum for a transform-limited input pulse and after several propagation distances following the reduced models of Eq. (4) (Kerr

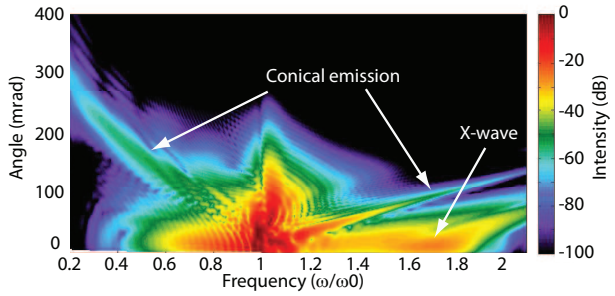

Figure 8: Angularly resolved pulse spectrum at the end of the fused silica plate.

effect only) , Eq. (5) (plasma only), and Eq. (6) (Kerr and plasma but no vibrational effects) are shown in Figures 9, 10, and 11, respectively.

4.3 Field encoding in the simulations

The encoding for the simulations was equivalent to the one used in the experiments (see Sec. 3.2) but using m=256 points (instead of m=16,384 as in the experiments). The total number of points m had to be reduced because some of the simulations were numerically expensive. Recall that the encoding consists in adding $f_1(s)$ and $f_2(s)$ to selected field's expectral components. More specifically, the encoding is given by

$$\varepsilon(\lambda, \mathrm{s_k}) = \begin{cases} \varepsilon(\lambda)\mathrm{e}^{\mathrm{i}f_1(\mathrm{s_k})}, & \text{if } \lambda \in [796.5 \text{ nm}, 798.5 \text{ nm}] \\ \varepsilon(\lambda)\mathrm{e}^{\mathrm{i}f_2(\mathrm{s_k})}, & \text{if } \lambda \in [787.5 \text{ nm}, 789.5 \text{ nm}] \\ \varepsilon(\lambda) & \text{otherwise} \end{cases}$$

The exact form of the encoding functions $f_1(s)$ and $f_2(s)$ can be computed following their definition given in 7 with m=256.

4.4 2D model

Here, we present the HE-OD calculations obtained with the full 2D+1 model, i.e using Eq. 1. Figure 12 shows the spectra obtained for all simulated experiments. It clearly appears that the output spectrum strongly depends on

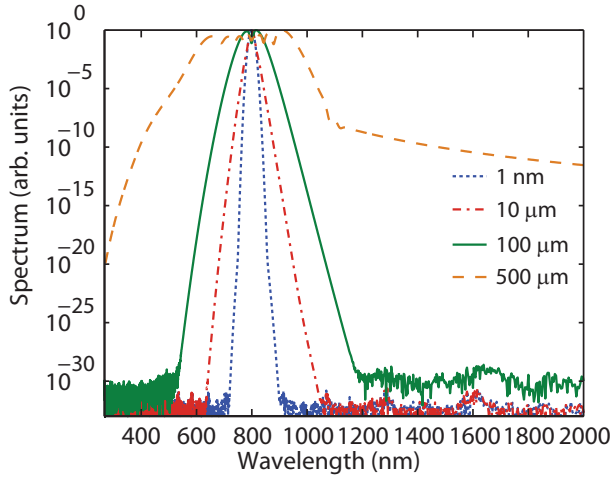

Figure 9: Spectrum of the Fourier transformed pulse for four propagation distances when considering Kerr effect only. Blue dots: 1nm, red dash-dots: 10 μm, solid green: 100 μm, and orange dash: 500 μm.

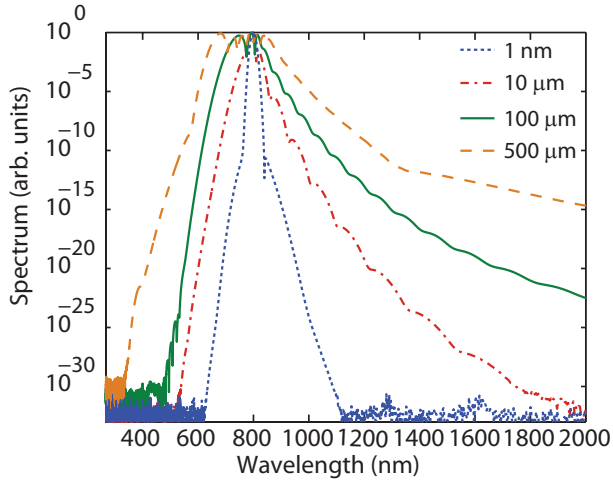

Figure 10: Spectrum of the Fourier transformed pulse for four propagation distances when considering plasma only. Blue dots: 1nm, red dash-dots: 10 μm, solid green: 100 μm, and orange dash: 500 μm.

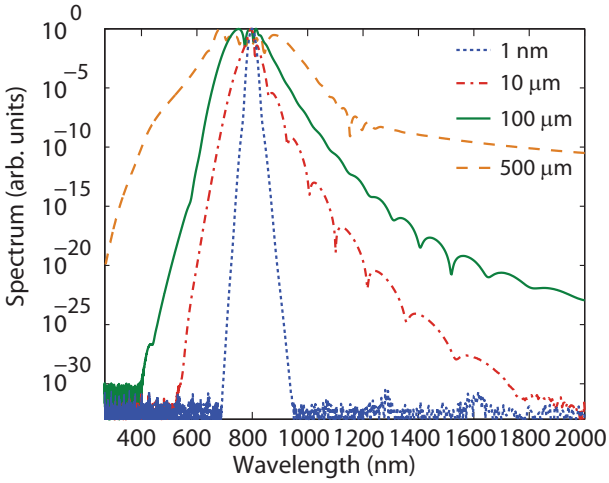

Figure 11: Spectrum of the Fourier transformed pulse for four propagation distances when considering Eq. 6 (both Kerr and plasma effects present). Blue dots: 1nm, red dash-dots: 10 μm, solid green: 100 μm, and orange dash: 500 μm.

the modulated phase applied to the initial pulse. In particular, one can show that the broadening is optimal when the applied phase are Φ_1=0.875π and Φ_2=1.125π respectively. This spectral dependence is linked to the optimal generation of the X-wave centered around $\lambda = 470$nm (between 400 nm and 530 nm depending on the experiment s_k) and propagating about 0.002 % slower than the main pulse.

More particularly, Fig.13 displays the output intensity of several spectral components (450, 520, 650 and 1600 nm respectively) as a function of the experiments s_k. It appears that these spectral components are not optimally generated for same encoding phase indicating distinct generation mechanisms.

In order to have a better look on the physical mechanism driving that phase dependence, Fig. 14 shows different properties of the pulse as a function of the experiments s. More particularly, Fig.14(a,b) show the maximal intensity and pulse radius respectively as a function of s, Fig.14(c-e) display the nonlinear phase shifts integrated over the whole propagation distance induced by bounded (Kerr), free (plasma) electrons and the sum of both contributions respectively. Finally, Fig. 14(f) shows the fluence averaged

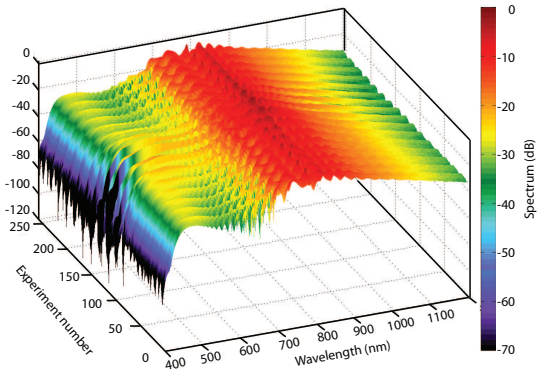

Figure 12: Simulated spectra of filaments after propagation in the fused silica plate as a function of the encoded field.

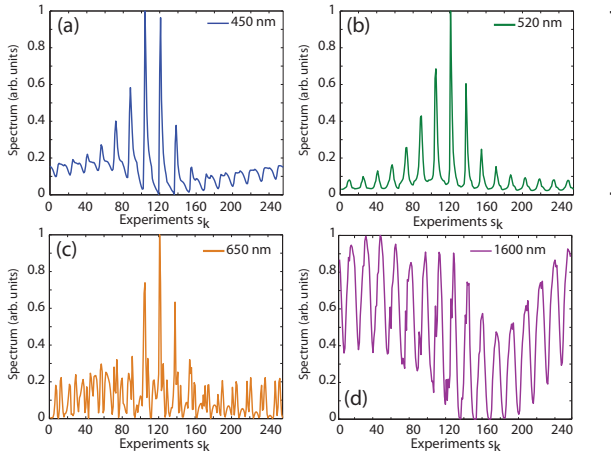

Figure 13: (a-d) Intensity of several on-axis spectral components (450, 520, 650, and 1600 nm respectively) at the end of the propagation for all experiments.

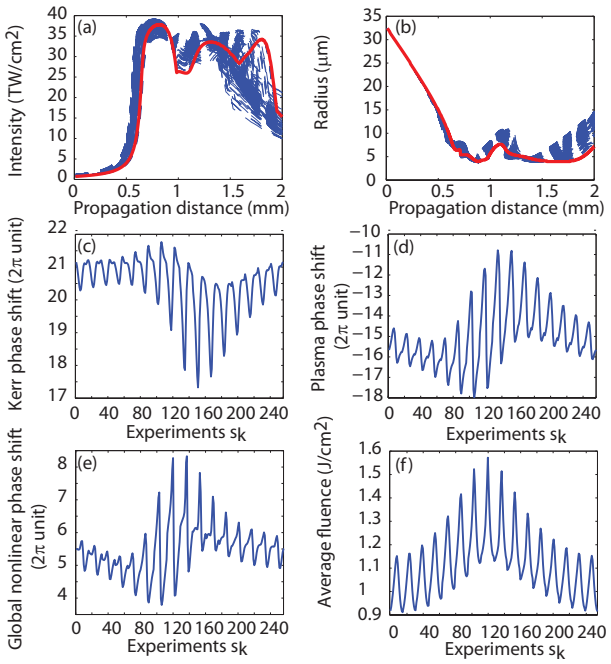

Figure 14: Panels (a) On-axis intensity and (b) pulse radius as a function of the propagation distance for every experiments respectively. The red curve corresponds to the experiment where the spectral broadening is optimal. (c-e) Kerr-induced (resp. plasma induced and global) nonlinear phase shift integrated over the propagation experienced by the pulses for all experiments. (f) Fluence averaged over the whole propagation for all experiments.

over the whole propagation distance.

The projections decoded from the modulated white light signal are shown in Figure 15.

4.5 1D model

In this section, we will consider a simple "1D" model in order to roughly catch the propagation dynamics of powerful laser pulse. This dimension-reduced model is particularly useful since it allows quick calculations compared with the full 2D+1 model. Let us consider that no space-time coupling occurs during the whole propagation, which then obeys Eq. 3. Even if this sim-

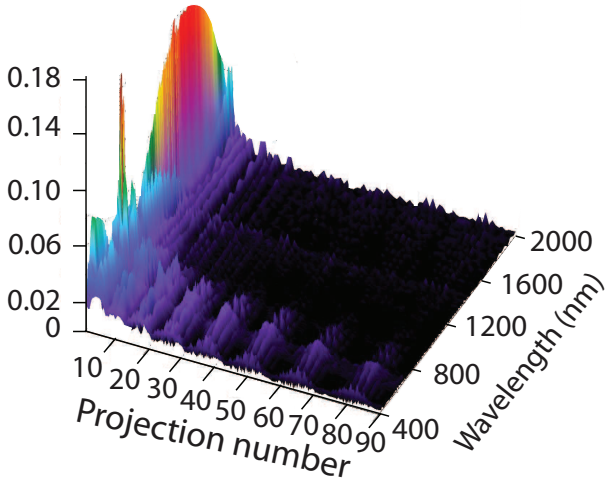

Figure 15: Field projection spectrum after propagation through the fused silica plate.

plification is not justified during the filamentation process, it allows to have a first look on the physics underlying the supercontinuum generation with short pulse.

The initial intensity of the Fourier transformed pulse is set at the level of the clamping intensity found with the help of the 2D calculations performed beforehand: I_0=35 TW/cm^2. Then the spectral coding is performed, reducing the peak intensity. In the following, we will highlight the contribution of each nonlinear effects on the projection spectrum.

4.5.1 Reduced model: Kerr effect and dispersion

We start our study with a reduced model taking into account dispersion and electronic Kerr effect only, neglecting any effect induced by free electrons or molecules vibration (Raman). Thus, the dynamics follow Eq. (4). The resulting simulated white light signal as a function of the encoding parameter s and wavelength is shown in Figure 16 for several propagation distances.

4.5.2 Impact of ionization on the HE-OD signal

Let us examine the impact of ionization on the HE-OD signal. For pulses intensities of about 30 TW.cm^{-2}, ionization is far from being negligible so that its effect on the propagation has to be taken into account. Let us first consider the effect of ionization alone on the HE-OD signal, i.e. neglecting both bounded electrons and vibrational effects. Accordingly, the the electric field propagation follows Eq. (5). The white light signal when only plasma effects are present as a function of the encoding parameter s and wavelength is shown in Figure 17 for several propagation distances.

4.5.3 HE-OD signal when considering Kerr effect and ionization

In the present section, we consider the propagation of the electric field influenced by both ionization and Kerr effect, neglecting only vibrational effects. In this case, Eq. (6) drives the electric field propagation. The white light signal neglecting vibrational effects as a function of the encoding parameter s and wavelength is shown in Figure 18 for several propagation distances.

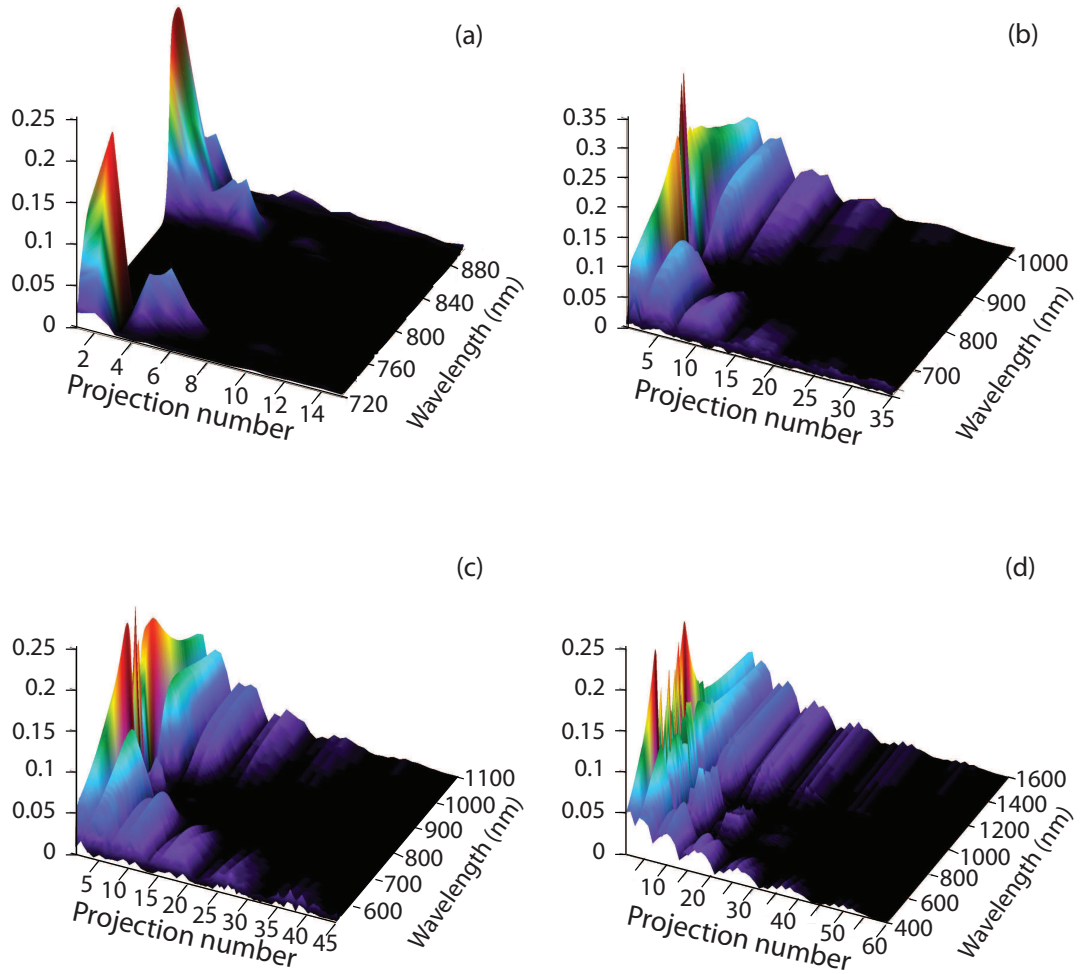

Figure 16: Field projection spectrum for four distinct propagation distances ((a) 1 nm, (b) 10 μm, (c) 100 μm, and (d) 500 μm) in fused silica of a 35 TW.cm^{-2}, 71.7 fs pulse when considering Kerr effect only.

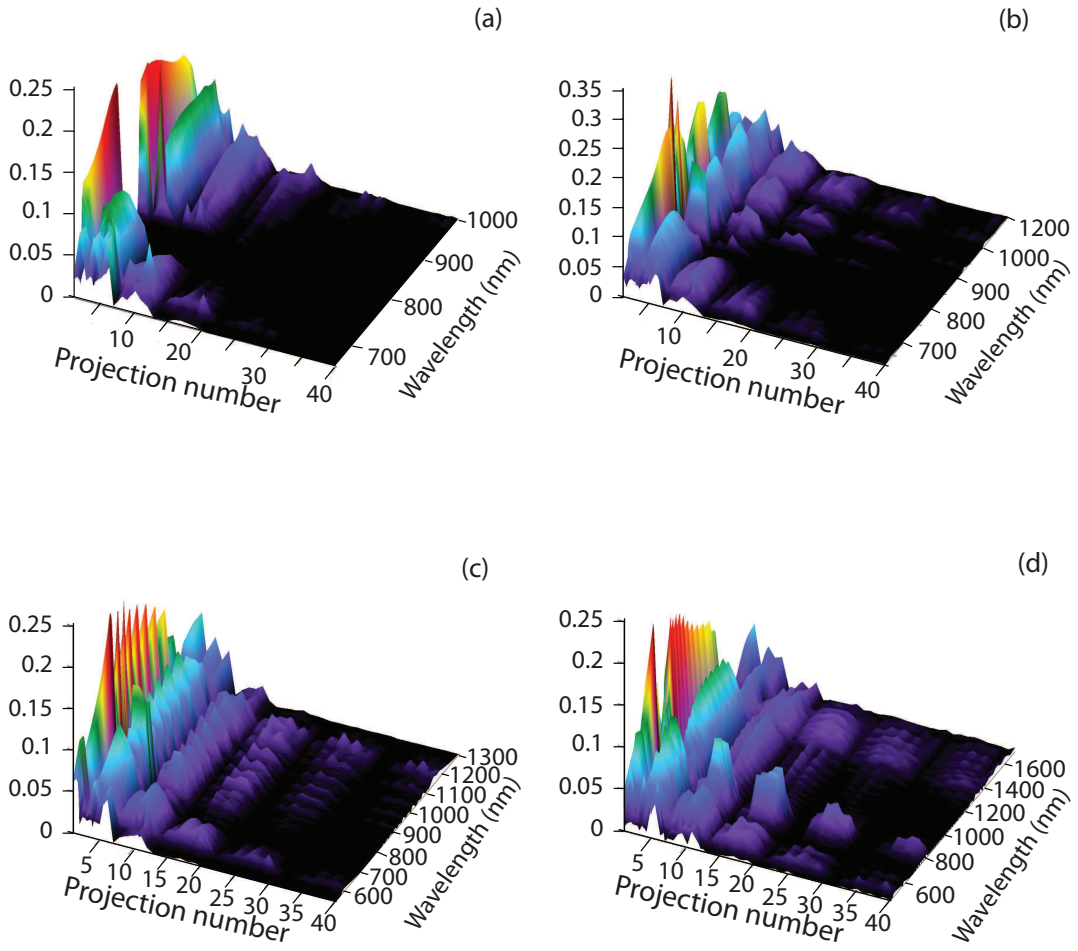

Figure 17: Field projection spectrum for four distinct propagation distances ((a) 1 nm, (b) 10 μm, (c) 100 μm, and (d) 500 μm) in fused silica of a 35 TW.cm^{-2}, 71.7 fs pulse when considering Eq.(5) (only plasma effects).

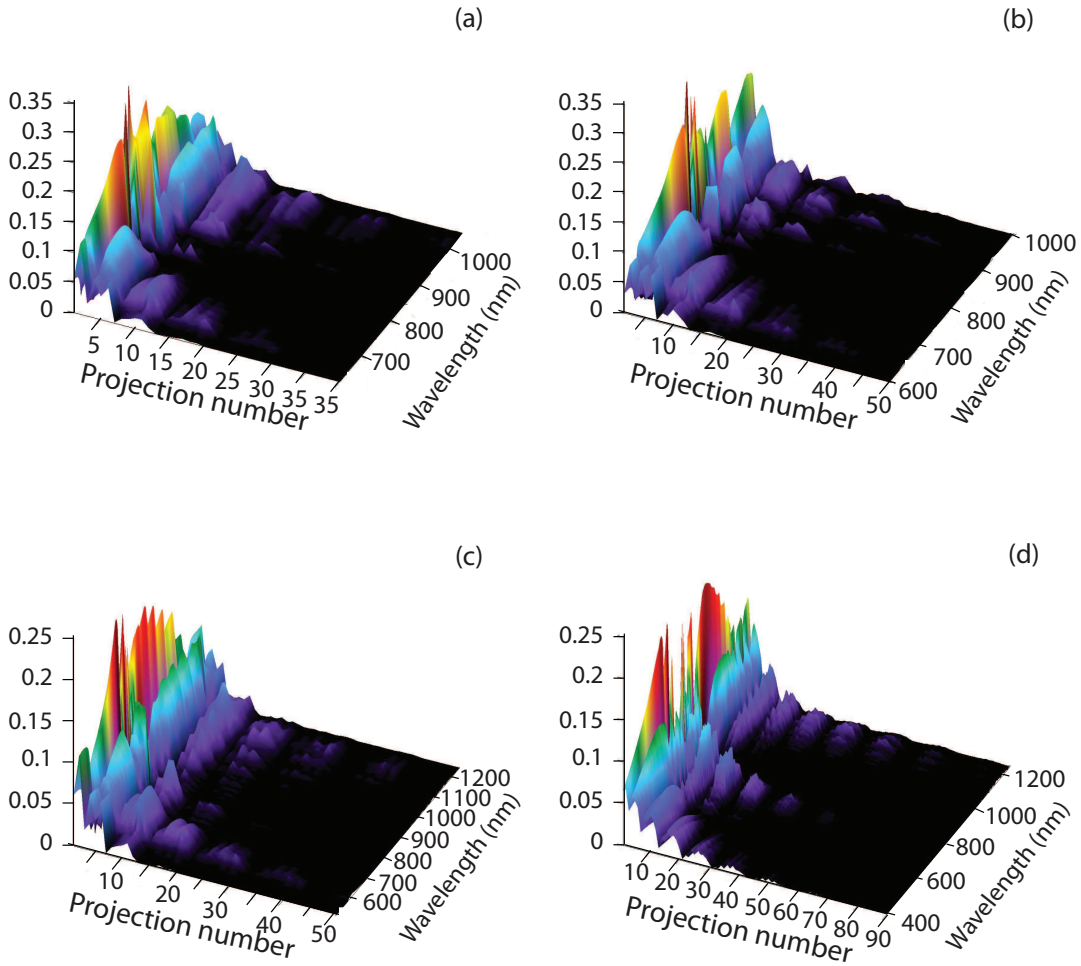

Figure 18: Field projection spectrum for four distinct propagation distances ((a) 1 nm, (b) 10 μm, (c) 100 μm, and (d) 500 μm) in fused silica of a 35 TW.cm^{-2}, 71.7 fs pulse when considering both Kerr and ionization.

5 Discussion

5.1 X-Wave interactions

A close analysis of the beam propagation properties illustrated in Figure 14 allows to underline the inherent mechanism of the white light generation. First, the higher frequencies of the spectrum (belonging to the second X-wave) are optimized when the global nonlinear phase shift is minimal (s=105). This optimization can be due to a better phase matching between the pump and the generated X-wave. Conversely, the generation of the green-red part of the spectrum is not linked to a nonlinear phase shift. Conversely, it is optimized when the filament carries an optimal energy (corresponding to the red solid curves (s=121) in Fig. 14(a,b)), i.e. when the fluence averaged over the propagation distance is optimal as one can notice in Fig. 14(f). This indicated that this spectral region (located between the fundamental part of the spectrum and the X-wave spectrum) is generated by a mixing between the X-wave and the fundamental pulse which is optimal when the filament is longer and carries more energy.

As shown in Fig. 19, the spectral dependence of the output pulse is linked with a strong temporal reshaping of the pulse. More particularly, the maximal spectral broadening is accompanied by the creation of a subpulse located at about 100 fs where the blue part of the spectrum (X-wave) is concentrated. Since this X-wave propagates with a smaller group velocity than the one centered at the fundamental wavelength, it is temporally delayed with respect to the fundamental at the end of the propagation.

Figure 15 shows the projection spectrum obtained at the end of the fused silica plate. As observed during experiments, high order projections are involved in the generation of the green-red part of the white-light. This is due to the inherent generation mechanism of this spectral region. Indeed, since it is generated by a nonlinear mixing between the fundamental and the X-wave, and consequently by cascading process (first, the X-wave is generated and it will in turn mixes with the fundamental), a wealth of high order projections are involved in the process.

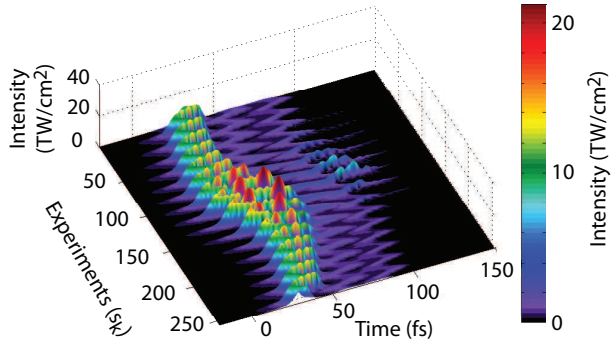

Figure 19: Simulated temporal profiles of filaments after propagation in the fused silica plate as a function of the encoded field.

5.2 Cascading mechanism for the high-order projections

Consider laser propagation under the influence of the Kerr effect only (see Sec. 4.5.1). In frequency space, the nonlinear polarization reads :

$$\mathrm{P_{NL}}(\omega) \propto \iint \widetilde{\varphi}^*(-\theta)\widetilde{\varphi}(\xi-\theta)\widetilde{\varphi}(\omega-\xi)d\xi d\theta \tag{13}$$

If one defines ω=ω_0+ν and considering an arbitrary frequency δ, the terms involving the encoded frequencies ω_1=$\omega_0 - \Delta\Omega$ and ω_2=$\omega_0 + \Delta\Omega$ are:

$$\begin{cases} \varepsilon(\omega_2+\nu+\delta)\varepsilon(\omega_1)\varepsilon^*(\omega_0+\delta) & \text{Projection (1,0)} \\ \varepsilon(\omega_1+\nu+\delta)\varepsilon(\omega_2)\varepsilon^*(\omega_0+\delta) & \text{Projection (0,1)} \\ \varepsilon(\omega_1)\varepsilon(\omega_2)\varepsilon^*(\omega_0-\nu) & \text{Projection (1,1)} \\ \varepsilon(\omega_1)\varepsilon(\omega_1+\nu-\Delta\Omega)\varepsilon^*(\omega_2) & \text{Projection (1,-1)} \\ \varepsilon(\omega_2)\varepsilon(\omega_2+\nu+\Delta\Omega)\varepsilon^*(\omega_1) & \text{Projection (-1,1)} \\ \varepsilon(\omega_1)\varepsilon(\omega_1)\varepsilon^*(\omega_2-\nu+\Delta\Omega) & \text{Projection (2,0)} \\ \varepsilon(\omega_2)\varepsilon(\omega_2)\varepsilon^*(\omega_1-\nu-\Delta\Omega) & \text{Projection (0,2)} \end{cases}$$

Consequently, at the very beginning of the propagation, only projections related to each of these terms are present in the decoding as one can notice in Fig. 16(a).

However, when the pulse propagates and spectrally broadens (Fig. 9), higher order projections grow up, as pictured in Fig. 16(b-d) which display spectral projections for a propagation distance of 10 μm, 100 μm and 500 μm respectively. Since no higher order nonlinear polarization is taken into account, these higher order projections can only be the signature of cascading third order processes. For instance, a frequency $\omega_0 + \gamma$ with $\gamma > \nu$ can be generated by the cascading third order process involving the frequency triplet $(\omega_1, \omega_1, \omega_0 + \nu)$ with $\nu = 2\Delta\Omega - \gamma$ and where $\omega_0 + \nu$ has been previously generated by a direct third order process involving the frequency triplet $(\omega_1, \omega_2, \omega_0 + \nu - \Delta\Omega)$. Accordingly, that particular frequency generation scheme will involve the projection (3,-1). As the pulse spectrum gets broader and broader and consequently, as soon as multiple cascading processes occur, projections of even higher-order will grow up. In particular, after 500 μm propagation, projections up to 65 is observed corresponding to the field projection (-4 , 4).

5.3 Plasma effects on the projection spectra

As one can notice in Fig. 17(a), even for very short propagation distances i.e. when no cascading process has occurred yet, the HE-OD signal consists of a wealth of projections orders, indicating that ionization is not proportional to any electric field order. More particularly, neglecting inverse Bremsstrahlung, electron recombination and photo-ionization losses, the propagation equation can be written in the frequency domain as :

$$\partial_z \widetilde{\varphi} = \mathrm{i}\left[\mathrm{k}(\omega) - \frac{\omega}{\mathrm{v_g}}\right]\widetilde{\varphi} + \frac{\mathrm{e}^2}{2\mathrm{n}(\omega)\epsilon_0 \mathrm{m_e c}}\tau(\omega)\frac{\sigma_\mathrm{K}}{\omega}\widetilde{|\varphi|^{2\mathrm{K}}} \otimes \widetilde{\varphi} \tag{14}$$

where $\otimes$ accounts for convolution and $\widetilde{|\varphi|^{2\mathrm{K}}} \otimes \widetilde{\varphi}$ can be written as:

$$\begin{aligned} \widetilde{|\varphi|^{2\mathrm{K}}} \otimes \widetilde{\varphi} &= \left(\bigotimes_{\mathrm{K}} \widetilde{|\varphi|^2}\right) \otimes \widetilde{\varphi} \\ &= \left(\bigotimes_{\mathrm{K\text{-}1}} \widetilde{|\varphi|^2}\right) \otimes \left(\widetilde{|\varphi|^2\varphi}\right) \quad . \end{aligned} \tag{15}$$

Consequently, it clearly appears that HE-OD signal at a given frequency ω will be made of the combination of a wealth of high order projections involving ω_1 and ω_2.

5.4 Kerr and plasma effects

Figure 18 displays the spectral HE-OD signal for four propagation distances. The HE-OD signal is composed of the combination of projection induced by bound electrons and free electrons. As a consequence, the HE-OD signal is made of plenty of field order projections which reflects that both cascading processes and ionization are not negligible. One can notice that higher order projections have a contribution centered around 600 nm for a propagation distance of 100 μm as observed experimentally.

6 Conclusions

In conclusion, we have numerically studied (with the help of both 1D+1 and 2D+1 simulations) the HE-OD signal during white light generation in fused silica. It appears that both plasma and Kerr effect can lead to higher order projections. While the former induces such higher order projections due to its highly nonlinear nature, the latter implies high order projections by cascading processes as the pulse spectrum gets broader and broader. This study also highlight the intrinsic spectral phase sensibility of white generation, and generally speaking of filamentation. This parametric study also exhibits the fact that filaments properties (temporal and spectral distributions, energy embedded in filaments, filament length and intensity,...) can be controlled with an appropriate pulse shaping and consequently opens the way to optimal control based filament experiments in bulk media.

7 Appendix

7.1 Orthogonal set of modulating functions

To generate an orthogonal set of modulating functions $\{h(r,q;s)\}$, begin by sampling an array $\{\phi_j\}$ of regularly-spaced phases in the interval $[0, 2\pi]$

$$\phi_j = 2\pi j/R \qquad , \; j = 0, \ldots, R-1 \tag{16}$$

where, R is a positive integer. The encoding functions $f_1(s)$ and $f_2(s)$ are constructed from a cartesian product of two phase arrays $\{\phi_j\}$:

$$f_1(1) = \ldots = f_1(R) = \phi_0,$$

$$f_1(R+1) = \ldots = f_1(2R) = \phi_1,$$
$$\vdots$$
$$f_1(m-R+1) = \ldots = f_1(m) = \phi_{R-1}.$$

And,

$$f_2(1) = \phi_0,\ f_2(2) = \phi_1, \ldots,\ f_2(R) = \phi_{R-1},$$
$$f_2(R+1) = \phi_0,\ f_2(R+2) = \phi_1, .., \ f_2(2R) = \phi_{R-1},$$
$$\vdots$$
$$f_2(m-R+1) = \phi_0,\ f_2(m-R+2) = \phi_1, \ldots,\ f_2(m) = \phi_{R-1}.$$

where, $m = R^2$.

Substituting $f_1(s)$ and $f_2(s)$ as defined above into the scalar product Eq. (**??**), gives

$$\begin{aligned} h(r,q;s) \circ h(r',q';s) &= \frac{1}{m} \sum_{s=1}^{m} e^{i[(r-r')f_1(s)+(q-q')f_2(s)]} \\ &= \frac{1}{R^2} \sum_{j,k=1}^{R} e^{i[(r-r')\phi_j+(q-q')\phi_k]} \\ &= \frac{1}{R^2} \left(\sum_{j=1}^{R} e^{i(r-r')\phi_j} \right) \times \left(\sum_{k=1}^{R} e^{i(q-q')\phi_k} \right) \\ &= \frac{1}{R^2} \left(\sum_{j=1}^{R} e^{i(r-r')2\pi j/R} \right) \times \left(\sum_{k=1}^{R} e^{i(q-q')2\pi k/R} \right) \end{aligned} \quad (17)$$

If $r = r'$ and $q = q'$, then the terms in the sumations in the RHS of Eq. 17 are all equal to 1, and therefore $h(r,q;s) \circ h(r',q';s) = 1$. Suppose instead that $r \neq r'$, then

$$\sum_{j=1}^{R} e^{i(r-r')2\pi j/R} = e^{i(r-r')2\pi/R}(1 - e^{i(r-r')2\pi})/(1 - e^{i(r-r')2\pi/R}) = 0,$$

for $|r| + |r'| \leq R/2$. The same holds for $q,$ and q'. We conclude that the set $\{h(r,q;s)\}$ is orthogonal

$$h(r,q;s) \circ h(r',q';s) = \delta_{r,r'}\delta_{q,q'}.$$

for $|r| + |r'|, |q| + |q'| \leq R/2$.

As a colorary, it may be possible to unambigously resolve a projection $P(r, q; T)$ from the experimental data only if $|r|, |q| \leq R/2$. Thus, the number of points R of the generating array $\{\phi_j\}$ has to be chosen so that the desired highest-order projections are resolvable.

References

[1] M. Kolesik and J. V. Moloney. nonlinear. *Phys. Rev. A*, 70:036604, 2004.

[2] A. Mitra and H. Rabitz. Identifying mechanisms in the control of quantum dynamics through Hamiltonian encoding. *Phys. Rev. A*, 67(3):33407, 2003.

[3] R. Rey-de Castro, Z. Leghtas, and H. Rabitz. Measuring and manipulating quantum control pathways on the fly. *Submitted to Phys. Rev. Lett.*, 2012.

[4] R. Rey-de Castro and H. Rabitz. Laboratory implementation of quantum-control-mechanism identification through Hamiltonian encoding and observable decoding. *Phys. Rev. A*, 81(6):63422, 2010.